Turkish Journal of Electrical Engineering & Computer Sciences

http://journals.tubitak.gov.tr/elektrik/

Research Article

Turk J Elec Eng & Comp Sci
(2022) 30: 659 – 677
© TÜBİTAK
doi:10.3906/elk-2104-73

Predictive optimization of sliding mode control using recurrent neural paradigm for nonlinear DFIG-WPGS during distorted voltage

Omar Busati Alzain[1,2,*], **Xiangjie Liu**[1]

[1]The State Key Laboratory of Alternate Electrical Power System with Renewable Energy Sources, School of Control and Computer Engineering, North China Electric Power University, Beijing, China,

[2]School of Electrical Engineering, Sudan University of Science & Technology, Khartoum, Sudan

Received: 11.04.2021 • **Accepted/Published Online:** 03.09.2021 • **Final Version:** 21.03.2022

Abstract: Dynamic characteristics of the doubly-fed induction generator (DFIG)-based wind power generation (WPGS) are fully nonlinear. Therefore, issues such as stability and achieving high efficiency, especially under harmonics behavior, are challenges that assess the control strategy reliability to find the perfect dynamic solution. This discussion offers a control strategy for the separated stator-port power using a predictive sliding mode strategy with a resonant function (PSMC-R) based on a deep recurrent neural network (DRNN). DRNN is formed as a low-order Taylor series formula. PSMC-R predicts the perfect switching surface path and regulates the distorted nonlinear DFIG with several dynamic aims. This approach reduces excessive chatter while violating the sliding surface path range of the classical SMC switch-part. Also, PSMC-R handled the fundamental and 5th-/7th-type harmonic wave at the positive synchronous +dq-reference level of the machine dynamic quantities without further dissociation computations of the components. Dynamic results of a 1.5 MW DFIG-WPGS are simulated by using Matlab-package and presented good dynamic characteristics, less pulsation ratio of variables, and optimal sliding chatter of PSMC-R during various operating scenarios compared to the other classical regulation approaches.

Key words: Double fed induction machine, wind engine unit, sliding surface controller, harmonic wave, regulation of power system

Nomenclatures

i_s, i_r	Stator- and rotor-port current vector.	P_s, Q_s and T_e	Stator-port active and reactive power and, machine electrical torque
v_s, v_r	Stator- and rotor-port voltage vector.	**Subscripts**	
ψ_s, ψ_r	Stator- and rotor-port flux vector.	α, β	Stationary level at α- and β-axis.
R_s, R_r	Stator- and rotor-port resistance.	d, q	Synchronous level at d-, q-axis.
L_m	Common-inductance.	s, r	Stator- and rotor-port variables.
L_s, L_r	Stator- and rotor-port inductances.	$+, 5-, 7+$	Positive-series of the primary + and 5 th/7th-degree harmonic items at $-5\omega_e$ and 7 ω_e.
$L_{\rho s}$, $L_{\rho r}$	Stator- and rotor-port outflow-inductances.	**Superscripts**	
ω_e	Stator angular speed.	r and $+, 5-, 7+$	Stationary level at $(\alpha\beta)^r$, and (+) synchronous reference level at $dq^{(}+, 5-, 7+)$.
ω_r, ω_s	Rotor-port, synchronous angular speed.	ref	Reference signal for controller.
θ_e, θ_r	Position angle of stator-, rotor-port.		

*Correspondence: omarbusati@ncepu.edu.cn, omarbusati@gmail.com

1. Introduction

Globally, the power generation based on wind-wave (WPG) has expanded rapidly within these years for growing global natural energy sources needs [1]. Flux and voltage orientation types of vector control are general strategies applied during the usual operating characteristics of DFIG-WPGS [2, 3]. WPGS is entirely nonlinear and unprotected from disturbance status types that decrease the system effectiveness, concerned classical controllers [4]. Accordingly, several topics have dealt with various enhanced control designs, such as a robust controller that has been analyzed in the stationary- or synchronous-level to improve the paradigm performance toward DFIG terminals [5, 6]. The optimization algorithm for the model predictive regulation approach (MPC) gives extensive regulation features to handle the DFIG. An optimum predictive voltage vector is derived based on the direct power control without the need to extract the negative chains of stator-port current to enhance its sequences and mitigate electromagnetic torque vibrations during an unbalanced network state [7]. Given the harmonics status, the predictive estimation compensator decreases the torque hesitation associated with stator-port current and flux [8]. The predictive regulation enhanced the torque and flux by adding ripple regulation term with the standard cost function to deal with torque ripple during an ineffective control action [9, 10]. MPC regulation-based stator-port current injected the predicted stator-port current at dq-plane to generate the rotor-port converter control signals without complex separations processes in the harmonic items. Which simplifies the regulation items, decreases the algorithm's burden, and enhances its dynamic robustness [11]. The sliding mode approach (SMC) is widely introduced to regulate the DFIG-WPG with unpredictable wind behavior, uncertainty changes, and external disturbances due to the insensitivity properties for unwanted dynamic deviations. SMC power regulation approach (SMC-DPC), using the influential extended power and adapted control based on the backward-steps procedure (ABS-SMC), is offered to deal with DFIG [12, 13]. Present network design recommends reducing the maintenance and operational costs and the possibility of overcoming malfunctions. The network-port is associated with the DFIG stator- and rotor-port through the transformer and dual-terminals converter, respectively, which may cause undesirable increases in rotor-port current. These dynamic challenges are influential for taking into account during advanced control design. Consequently, additional smart control approaches have been proposed to discuss DFIG behaviour under unusual voltage dips conditions [14–17]. The SMC model deals effectively with the applicable system during these cases due to its rapid reaction to correct unwanted dynamic perturbations[18, 19]. A high-degree SMC has been offered for the DPC toward DFIG's terminals [20] and speed-control toward turbine (WT) [21]. The Integral I-SMC directly controlled the DFIG's torque under unbalanced system voltage that alleviates the ripples impact on the torque and stator-port power in [22]. An I-SMC-based torque control manipulated voltage drop effects and reduced the vibration of stator-port power and mechanical torque (MT) for the DFIG system. Also, DPC strategy-based DFIG regulation via I-SMC has regulated the stator-port power and compensated the power oscillations using resonant units running at a double value of actual frequency [23]. Three regulation targets that have been adopted depend on the current of the stator-port, power during the stable condition, and damped vibrations of MT. The study in [14] offered ISMC-DPC with two scenarios, such as collapse and distortion in the network-area voltage, for mitigating the dynamic harmonic effects on the DFIG. The actual behavior of the nonlinear and inductive effect of the power system equipment, with power electronics converters units leads to the emergence of harmonics sequences, which causes a significant change in the fundamental sinusoidal wave structure of system variables, especially the $5^{th}/7^{th}$-degree of harmonic. The appearance of harmonious fluctuations in the power feed unit results in MT vibration and high energy dissipation through the machine core. The electrical communities have identified standards for reducing harmonic ratios on acceptable operational limits along the generation line, and the most famous are IEEE-519 and ERG5/4-1 [18]. In [23, 24], I-SMC with multi-resonance elements suppressed the harmonic effect and restricted the tracking deviation of DFIG variables sequences that may be present under unusual network voltage conditions. The multi-resonant integral law modified the sliding surface elements based on the SMC approach to manipulate the deformed voltage at the positive dq-reference-level. This strategy provided good tracking behavior and attenuated the oscillation on the stator-port power and response of MT for the DFIG [25]. Generally, the stable and transient behavior of DFIG has been regulated during the normal and abnormal operating conditions in previous studies without providing a more detailed analysis of the effect of different kinds of harmonics. The previous SMC regulation investigations frequently presented the classical chattering signal based on their sliding quantities, signs, and restrictions that may affect sliding behavior on the efficient surface to realize dynamic targets. This paper presents PSMC-R utilizing the predictive sliding chattering signals based on a deep recurrent neural network (DRNN) of the DFIG-WPG stator-port power under $5^{th}/7^{th}$-degree harmonic related to voltage. The PSMC-R has a sliding formula like an ordinary PI structure which contains a predictive sliding term, with the addition of resonant compensator unit oscillated at 6-times the feeder frequency. The required stator-port power is necessary to derive many control characteristics with different modes of operation. The results show that the PSMC-R control presents the best dynamic tracking, low overshoot, and fluctuation of electrical quantities compared to SMC, PI, and PIR controllers during various operation cases. Moreover, the frequency of stator/rotor-port sinusoidal current wave has remained constant.

2. DFIG-WPGS structure representation

2.1. Mathematical description of DFIG

The transient circumstances of the DFIG are complicated for design due to the influence of the variations on the inner parameters, such as coil inductance and stator- and rotor-port resistors associated with the inherent variations in magnetic fields. Thus, as displayed in Figure 1, the DFIG as an uncomplex corresponding circuit can be deduced based on some propositions for the usual- and distorted voltage running conditions. The initial proposition considers that the nonlinear sequences of DFIGs can be extracted based on the $(+)$ synchronous scheme $(dq)^+$ related to angular speed $\omega = \omega_e$. In addition, the $+$ harmonic progressions items (HPI) on the main variables are shaking at $-5\omega_e$ and $7\omega_e$ as revealed in Figure 2. The rated values of the system are calculated along per unit scale (pu). Also, assuming the machine structure that includes the airflow is a symmetrical structure to idealize the DFIG circuit. In general, the stationary-references $(\alpha\beta)$ of the DFIG dynamic quantities (F) were specified as following [26]:

$$F_{\alpha\beta} = F_{\alpha\beta+} + F_{\alpha\beta5-} + F_{\alpha\beta7+} \quad = \left|F_{\alpha\beta+}\right|.e^{j\phi1} + \left|F_{\alpha\beta5-}\right|.e^{-j\phi5} + \left|F_{\alpha\beta7+}\right|.e^{j\phi7} \tag{1}$$

where $\phi1 = \omega_e.t + \varphi_+, \phi5 = 5\omega_e.t + \varphi_5$ and $\phi7 = 7\omega_e.t + \varphi_7$, also, φ_+, φ_5 and φ_7 are the primary phase retards that belong to the $(+)$ components of the basic items (BSI) and HPI which are shaking at $(5, 7)$ feeder frequency, respectively. The phase beams indicated the link between the stationary, rotational and synchronous levels of BSI and HPI for electrical DFIG variables as in Figure 2. Moreover, the map shows that the $+d$–arrow is settled on $(+)$–arrow stator voltage sequences that operate at ω_e. d-arrow of $(dq)^{5-}$ and $(dq)^{7+}$ at $-5\ \omega_e/7\ \omega_e$ are spaced from α-arrow by $-\theta_5$ and θ_7, respectively. Derivation of the transformational relationship between the stationary level at $(\alpha\beta)$ and $(\alpha\beta)^r$, and synchronous level at$(dq)^{+,5-\ and\ 7+}$ with indicators r,+,

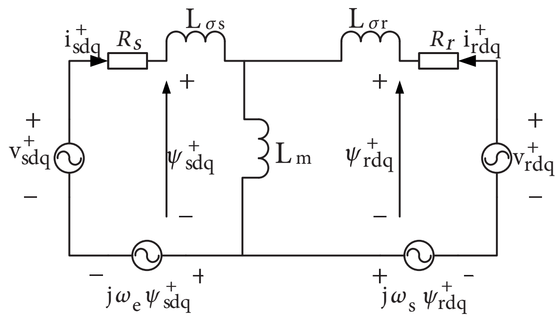

Figure 1. Equivalent paradigm of the DFIG at dq^+-level.

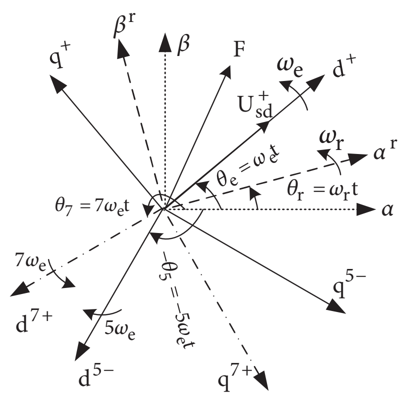

Figure 2. Orientation phasor analysis during the distorted stator-port voltage.

5− and 7+, respectively, are formulated as:

$$\begin{array}{lll} F^+_{dq} = F_{\alpha\beta}\mathrm{e}^{-j\omega_e t}, & F^{5-}_{dq} = F^{7+}_{dq}\mathrm{e}^{j12\omega_e t}, & F^+_{dq} = F^r_{\alpha\beta}\mathrm{e}^{-j(\omega_e-\omega_r)t} \\ F^{5-}_{dq} = F_{\alpha\beta}\mathrm{e}^{j5\omega_e t}, & F^+_{dq} = F^{5-}_{dq}\mathrm{e}^{-j6\omega_e t}, & F^{5-}_{dq} = F^r_{\alpha\beta}\mathrm{e}^{j(5\omega_e+\omega_r)t} \\ F^{7+}_{dq} = F_{\alpha\beta}\mathrm{e}^{-j7\omega_e t}, & F^+_{dq} = F^{7+}_{dq}\mathrm{e}^{j6\omega_e t}, & F^{7+}_{dq} = F^r_{\alpha\beta}\mathrm{e}^{-j(7\omega_e-\omega_r)t} \end{array} \tag{2}$$

In Figure 1, the complex relationships referred to as $+dq$-reference level can be designed similar to approach into [4]. Thus, DFIG dynamics are determined to correspond to the relationships between stator/rotor-port voltages, the passed current in impedances and fluxes, v^+_{sdq}, v^+_{rdq}, $i^+_{sdq}, i^+_{rdq}, \psi^+_{sdq}$ and ψ^+_{rdq} respectively [27].

$$\begin{aligned} v^+_{sdq} &= R_s i^+_{sdq} + \frac{d\psi^+_{sdq}}{dt} + j\omega_e \psi^+_{sdq} \\ v^+_{rdq} &= R_r i^+_{rdq} + \frac{d\psi^+_{rdq}}{dt} + j\left(\omega_e - \omega_r\right)\psi^+_{rdq} \end{aligned} \tag{3}$$

$$\begin{aligned} \psi^+_{sdq} &= L_s i^+_{sdq} + L_m i^+_{rdq} \\ \psi^+_{rdq} &= L_m i^+_{sdq} + L_r i^+_{rdq} \end{aligned} \tag{4}$$

where $L_s = L_{\rho s} + L_m$, $L_r = L_{\rho r} + L_m$ and $L_{\rho s}$, $L_{\rho r}$, and L_m are the stator-port/rotor-port outflow-, and common-inductances impact, respectively. The nominated general expression of DFIG variables is imputed to $+dq$-reference conditions of the basic and harmonic sequences along two frequencies ($5\ \omega_e$ and $7\omega_e$) with the Equations (1) and (2) as follows:

$$F^{+}_{\substack{sdq\\rdq}} = F^{+}_{\substack{sdq+\\rdq+}} + F^{+}_{\substack{sdq5-\\rdq5-}} + F^{+}_{\substack{sdq7+\\rdq7+}} = F^{+}_{\substack{sdq+\\rdq+}} + F^{5-}_{\substack{sdq5-\\rdq5-}}.e^{-j6\omega_e t} + F^{7+}_{\substack{sdq7+\\rdq7+}}.e^{j6\omega_e t} \tag{5}$$

where the + chains of the basic and the harmonic rippled at $-5\ \omega_e$ and $7\omega_e$ were assigned by $+$, 5, and $7+$ respectively. It can be considered that the behavior of the harmonious waves that are combined together similar to a frequency AC wave hesitating at $\pm 6\ \omega_e$ in dq^{+}-plane. Also, present the $5^{th}/7^{th}$-degree of stator/rotor-port harmonics at the $(dq)^{5-}/(dq)^{7+}$ respectively. The nonlinear variables of the stator/rotor-port can be obtained from Equations (3),(4) and (5), and reshaping the stator/rotor-port fluxes computations as in [27]:

$$\begin{aligned}
di^{+}_{sd}/dt &= H_1 i^{+}_{sd} + H_2 i^{+}_{sq} + H_3 i^{+}_{rd} + H_4 i^{+}_{rq} + n_1 v^{+}_{sd} + n_2 v^{+}_{rd}\\
di^{+}_{sq}/dt &= H_5 i^{+}_{sd} + H_6 i^{+}_{sq} + H_7 i^{+}_{rd} + H_8 i^{+}_{rq} + N_1 v^{+}_{sq} + N_2 v^{+}_{rq}\\
di^{+}_{rd}/dt &= G_1 i^{+}_{sd} + G_2 i^{+}_{sq} + G_3 i^{+}_{rd} + G_4 i^{+}_{rq} + M_1 v^{+}_{sd} + M_2 v^{+}_{rd}\\
di^{+}_{rq}/dt &= G_5 i^{+}_{sd} + G_6 i^{+}_{sq} + G_7 i^{+}_{rd} + G_8 i^{+}_{rq} + M_1 v^{+}_{sq} + M_2 v^{+}_{rq}\\
d\omega_s/dt &= PL_m/J\ (i^{+}_{sq} i^{+}_{rd} - i^{+}_{sd} i^{+}_{rq}) - T_m/J
\end{aligned} \tag{6}$$

where

$H_1 = \frac{-R_s}{L_s\sigma}$ $\quad H_2 = +\sigma^{-1}\frac{\omega_e-\omega_s L_m^2}{L_s L_r}$ $\quad H_3 = \frac{R_r L_m - L_r L_m}{L_s L_r - L_m^2}$ $\quad H_4 = -\frac{\omega_s L_m}{L_s\sigma}$ $\quad H_5 = -\sigma^{-1}\frac{\omega_e-\omega_s L_m^2}{L_s L_r}$ $\quad H_6 = \frac{-R_s}{L_s\sigma}$

$H_7 = +\frac{\omega_s L_m}{L_s\sigma}$ $\quad H_8 = \frac{R_r L_m - L_r L_m}{L_s L_r - L_m^2}$ $\quad G_1 = \frac{-R_s L_m}{L_s L_r\sigma}$ $\quad G_2 = -\frac{(\omega_e-\omega_s)L_m}{L_r\sigma}$ $\quad G_3 = -\frac{R_r L_s - L_m^2}{L_s L_r - L_m^2}$ $\quad G_4 = +\frac{\omega_s}{\sigma}$

$G_5 = +\frac{(\omega_e-\omega_s)L_m}{L_r\sigma}$ $\quad G_6 = \frac{-R_s L_m}{L_s L_r\sigma}$ $\quad G_7 = -\frac{\omega_s}{\sigma}$ $\quad G_8 = -\frac{R_r L_s - L_m^2}{L_s L_r - L_m^2}$ $\quad N_1 = \frac{1}{L_s\sigma}$ $\quad N_2 = \frac{L_m}{L_s L_r - L_m^2}$

$M_1 = \frac{-L_m}{L_s L_r\sigma}$ $\quad M_2 = \frac{-L_m^2}{L_s L_r^2\sigma}$ $\quad \sigma = 1 - L_m^2/L_s L_r$.

As equivalent approach in [26] and for the regulation design target, the v^{+}_{sd} coordinate is assumed to be equal to stator-port voltage u_s as fixed unity value and, stator-port power and the generator-torque are specified as

$$\begin{pmatrix} Ps^{+} \\ Qs^{+} \end{pmatrix} = {}^{3}/_{2} \begin{pmatrix} \mathrm{Re}\{v^{+}_{sdq}.\hat{I}^{+}_{sdq}\} \\ \mathrm{Im}\{v^{+}_{sdq}.\hat{I}^{+}_{sdq}\} \end{pmatrix} \overset{def}{=} {}^{3}/_{2} \begin{pmatrix} u_s i^{+}_{sd} \\ -u_s i^{+}_{sq} \end{pmatrix} \tag{7}$$

$$T_e = 3pL_m.\,\mathrm{Im}\{\psi^{+}_{sdq}.\hat{I}^{+}_{rdq}\} \tag{8}$$

where $\hat{I}^{+}_{sdq}$ is a convoluted conjugate space vector of the stator-port current.

3. Control mechanism representation

3.1. Neural network mechanism structure

The regulation model is executed using standard SMC based on a predictive neural network with adding a resonant harmonic part (PSMC-R) adapted at 6-times feeder frequency as shown in Figures 3-4.

It may be noted that the regular compensation unit (Rc) is a dual-action Integrator unit [28, 29]. Accordingly, the PSMC-R with a predicted sliding region for the stator-port power in *dq*-reference level can be developed to restrain the + main and $5^{th}/7^{th}$-degree harmonic items. According to the DRNN structure in [30, 31], the dynamic sequences of the DFIG system in Equations (6) and (7) can be formed as a nonaffine NARX structure *fa* (nonlinear auto-regressive eXogenous) based DRNN:

$$\bar{y}_{k+1} = f_a(\varphi_k, \varepsilon) \tag{9}$$

where the label ε is white unevaluated noise. The regression arrays can be defined as $\varphi_k = [\bar{y}_{k+p-1}, ..., \bar{y}_{k+p-m_y}, u_k, ..., u_{k-m_u+1}]$ which uses absolute coefficients m_y and m_u to limit the regression vector depending on the

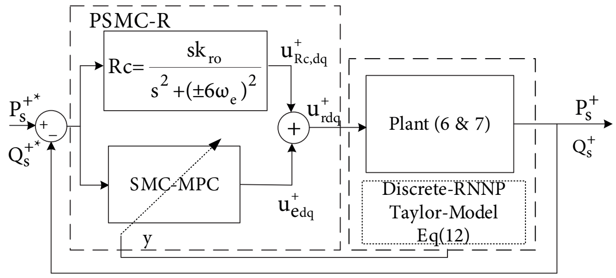

Figure 3. PSMC-R model of stator-port power control.

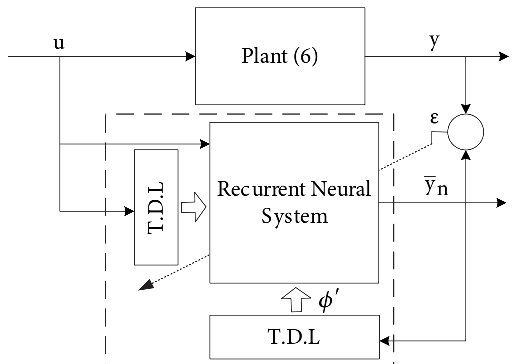

Figure 4. The equivalent trained DRNN model of DFIG at $+dq$ reference status.

previous shifted output $(\bar{y})$/input (u) information. The new NARX affine form can be built using interior regression array and input elements u_k as: $\varphi_k = [\varphi'_k, u_k]$. where $\varphi'_k = [\bar{y}_{k+p-1}, ..., \bar{y}_{k+p-q_y}, u_{k-1}, ..., u_{k-q_u+1}]$.

$$\varphi'_{k+1} = f_x(\varphi') + g_u(\varphi').u_k + \bar{\omega}, \qquad \bar{y}_k \quad = h_y(\varphi') \tag{10}$$

where f_x, g_u and h_y are specified as DRNNs input and output components, also $\bar{\omega}$ is unmeasured disturbances. By restructuring DRNNs Equation (10) to be similar to the low-rank of Taylor multi-series at the operation points $[\varphi'_0(k)]$ that is defined as previous sequences of input/output.

$$\begin{aligned}
\varphi'(k+1) &= f_x(\varphi'_0(k)) + \left(\frac{\partial f_x(\varphi')}{\partial \varphi'}\bigg|_{\varphi'_0(k)}\right)(\varphi' - \varphi'_0) + \left(\frac{\partial g_u(\phi')}{\partial u}\bigg|_{\varphi'_0(k)}\right)(u - u_0) + \bar{\omega} \\
\Delta\varphi'_{k+1} &= \hat{A}.(\varphi' - \varphi'_0) + \hat{B}.(u - u_0) + \delta_k \\
\bar{y}(k) &= h_y(\varphi'_0(k)) + \left(\frac{\partial h_y(\varphi')}{\partial \varphi'}\bigg|_{\varphi'_0(k)}\right)(\varphi' - \varphi'_0) \\
\Delta\bar{y}_k &= \hat{C}.(\varphi' - \varphi'_0)
\end{aligned} \tag{11}$$

where $\Delta x = \Delta\varphi' = (\varphi' - \phi'_0)$ and $\Delta u = (u - u_0)$. The new linear matrices are represented as $\hat{A} = \frac{\partial f_x}{\partial \varphi'}\Big|_{\varphi'_0}$, $\hat{B} = \frac{\partial g_u}{\partial u}\Big|_{\varphi'_0}$ and $\hat{C} = \frac{\partial h_y}{\partial \varphi'}\Big|_{\varphi'_0}$. In general, the model Equation (6) is formulated as linear steady-state form based on a low-degree Taylor approximation sequence around known processing points Equation (11):

$$\begin{aligned} \Delta x_{k+1}^{+} &= \hat{A}\Delta x_k^{+} + \hat{B}\Delta u_k^{+} + \delta_k^{+} \\ \Delta y_k^{+} &= \hat{C}\Delta x_k^{+} \end{aligned} \tag{12}$$

This investigation offered 3-steps affine shifted structure of the DRNN based on Figure 4. A set of dynamic data are generated using MATLAB open-platform (FAST-Tool) for WPGS, as presented in Figure 5. This platform is provided by the American National Renewable Energy Laboratory (NREL). FAST-Tool trains the model Equation (11) with the controller inputs as rotor voltage signals. Figure 6 shows the unit scale system data applied to learn the DRNN as an accurate affinity formula in a sampling time. In addition, the flow-chart of PSMC-R design based on DRNN, prediction routine, and SMC are presented in Figure 7.

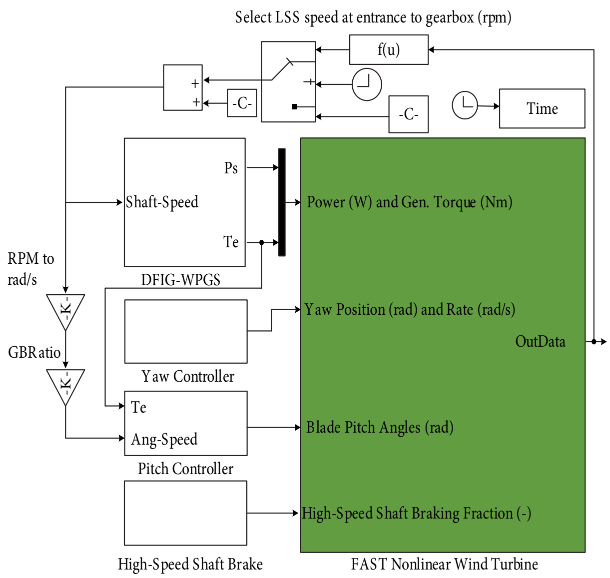

Figure 5. The FAST-based wind turbine model.

3.2. PSMC-R mechanism structure

Most earlier studies presented a discrete-time sliding structure with a sliding surface scheme using a proportional or an integral part law, which is defined using system variables, or sometimes the sliding range is designed to be a specified path [32–34]. In this study, the sliding law is identified like the PI formula to find the optimal control action, and the state error is set as

$$\Delta e_k^{+} = \Delta x_k^{+} - \Delta x_k^{ref} \tag{13}$$

where x_k^{*} is the signal of the expected input. Sliding-surface function (s) can be described as PI formula

$$\Delta s_{k+1}^{+} = k_P.\Delta e_{k+1}^{+} + k_I.\Delta \xi_{k+1}^{+} \tag{14}$$

The h-plane of sliding chatter path $s^{+} = \{s_{k-1}^{+} | s_{k-1}^{+} = 0, \text{ at k} = 1, 2, ...\}$, and the integration deviation is

$$\Delta \xi_k^{+} = \Delta e_k^{+} + \Delta \xi_{k-1}^{+} \tag{15}$$

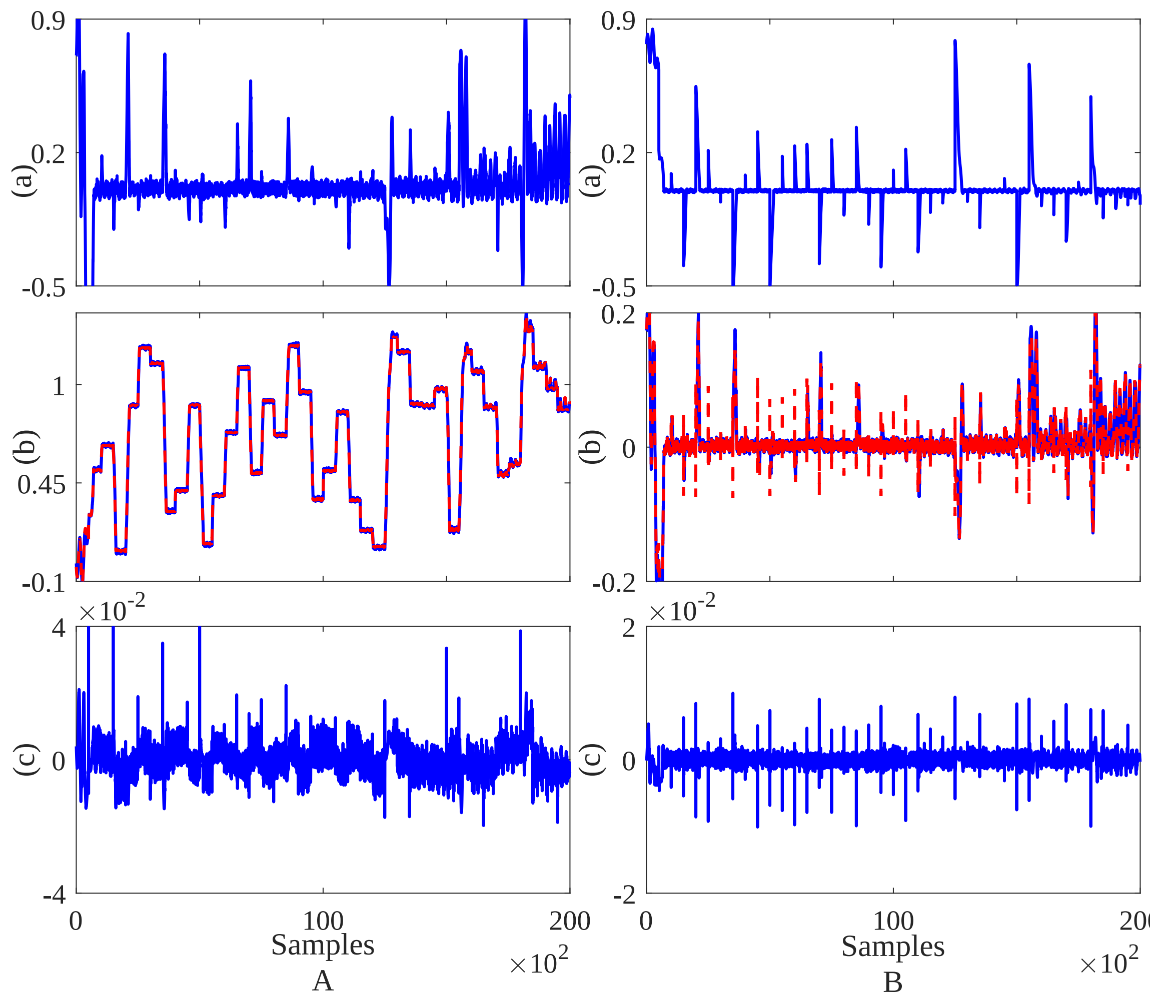

Figure 6. The training steps of the DRNN as (a) random data of inputs, (b) the DRNN verification for $+dq$-(solid-plant) and (dashed-trained data) and (c) the predicted errors. (A) $+d$-axes of the stator-port current. (B) $+q$-axes of the stator-port current.

Replacing Equation (12) into Equation (13)

$$\Delta e_{k+1}^{+} = \Delta x_{k+1}^{+} - \Delta x_{k+1}^{ref} = \hat{A}\Delta e_k^{+} + \hat{B}\Delta u_k^{+} + \underset{\sim k}{d^{+}}, \quad \underset{\sim k}{d^{+}} = \delta_k^{+} - \Delta x_{k+1}^{ref} + \hat{A}\Delta x_k^{ref} \tag{16}$$

The identical control signal Uc^{+} is offered to be a solution at $\Delta s^{+} = \Delta s_{k+1}^{+} - \Delta s_k^{+} = 0.$ [35]

$$\begin{aligned} \Delta s_k^{+} &= k_P e_{k+1}^{+} + k_I.\left(e_{k+1}^{+} + \xi_k^{+}\right) = \left(k_P + k_I\right)\Delta e_{k+1}^{+} + k_I.\Delta\xi_k^{+} \\ &= G_m.\Delta e_{k+1}^{+} + k_I.\Delta\xi_k^{+} \end{aligned} \tag{17}$$

Reforming Equation (17) based on Equation (16) to find the sliding term array as

$$\Delta s_k^{+} = G_m.\left(\hat{A}\Delta e_k^{+} + \hat{B}\Delta U_{c,k}^{+} + \underset{\sim k}{d^{+}}\right) + k_I.\Delta\xi_k^{+} \tag{18}$$

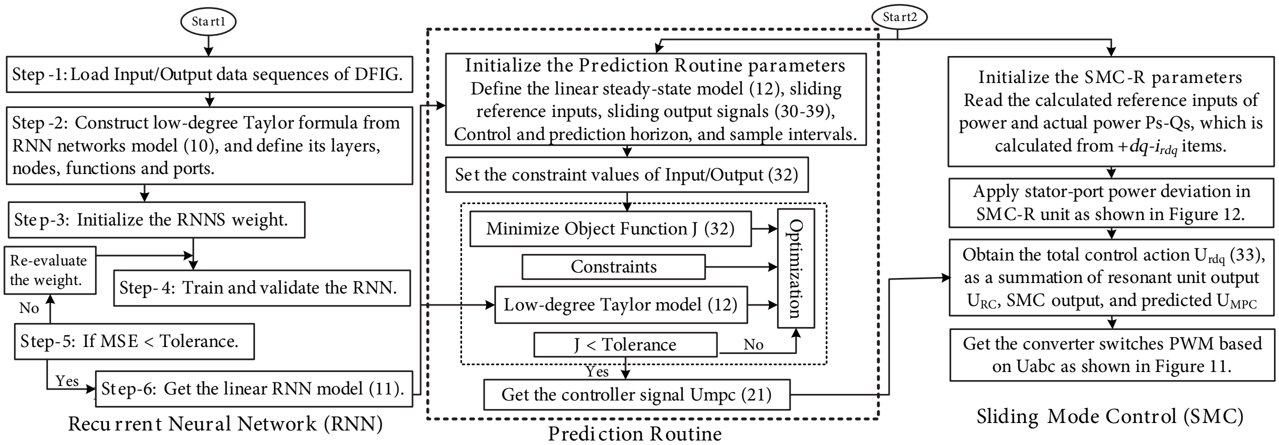

Figure 7. Flow-chart of the PSMC-R design based on DRNN.

The applied identical control comprises a one-ahead shift disturbance that can be formed as

$$\Delta U^+_{c,k} = -\left(G_m \hat{B}\right)^{-1}\left(-\Delta s^+_k + G_m \hat{A}\Delta e^+_k + G_m \underset{\sim k-1}{d^+} + k_I \Delta\xi^+_k\right) \tag{19}$$

Redefine the sliding sequence as $s^+_{k+1} = s^+_k = 0$. Thus, Equation(19) is determined as

$$\Delta U^+_{c,k} = -\left(G_m \hat{B}\right)^{-1}\left(G_m \hat{A}\Delta e^+_k + G_m d^+_{k-1} + k_I \Delta\xi^+_k\right) \tag{20}$$

This investigation uses the predicted switching-part based on predictive control (pc) instead of the common switching-part of SMC $\Delta U_{sw,k} = \mathrm{K}_m sign\left(\Delta s\right) + \eta\Delta s$ to extend the functional control space and coerce the system states to realize the sliding attributes. Consequently, the general formula of control action can be expressed as

$$\Delta U^+_k = \Delta U^+_{c,k} + \Delta U^+_{sw,k} = \Delta U^+_{c,k} + \Delta U^{pc,+}_k \tag{21}$$

The border layer $\bar{\Delta}$ is described for constricting the state of chatter as follows

$$\begin{cases} 1, & s^+ > \bar{\Delta} \\ \mathrm{ks}, & \left|s^+\right| \le \bar{\Delta}, \quad k = 1/\bar{\Delta} \\ -1, & s^+ < -\bar{\Delta} \end{cases} \tag{22}$$

Thus,

$$\Delta U^+_k = -\left(G_m.\hat{B}\right)^{-1}\left[-\Delta s^+_k + G_m \hat{A}\Delta e^+_k + G_m \underset{\sim k-1}{d^+} + k_I \Delta\xi^+_k + G_m\left(k_m sign\left(\Delta s^+_k\right) + \eta.\Delta s^+_k\right)\right) \tag{23}$$

Replacing Equations (23), (21) into Equation (18), the future sequences of sliding term can be composed as

$$\Delta s^+_{k+1} = G_m.\left(\hat{A}\Delta e^+_k + \hat{B}.\left(\Delta U^+_{c,k} + \Delta U^{+,pc}_k\right) + \underset{\sim k}{d^+}\right) + k_I.\Delta\xi^+_k \; = \Delta s^+_k + G_m \hat{B}\Delta U^{+,pc}_k + G_m \underset{\sim k}{\varepsilon^+} \tag{24}$$

$\underset{\sim k}{\varepsilon^+} = \underset{\sim k}{d^+} - \underset{\sim k-1}{d^+}$ is an approximated error vector representing the disturbance under restriction

$$\left|\underset{\sim k}{\varepsilon^+}\right| = \underset{\sim k}{d^+} - \underset{\sim k-1}{d^+} \le \hat{\Delta}_d \tag{25}$$

As indicated in Equation (24) with setting $\Delta\bar{u}^{+}(k) = \Delta U_{k}^{+,pc}$, the sliding status is expressed compactly as

$$\Delta s_{k+1}^{+} = \Omega.\Delta s_{k}^{+} + \Phi.\Delta\bar{u}_{k}^{+} + \Gamma \underset{\sim k}{\varepsilon^{+}}, \qquad \underset{\sim k}{y^{+}} = H\Delta s_{k}^{+} \tag{26}$$

In Equation (26), the constant matrices are expressed as
$\Omega = [I] = \begin{bmatrix}1 & 0\\ 0 & 1\end{bmatrix}$, $\Phi = \begin{bmatrix}G_m\hat{B}\end{bmatrix} = \begin{bmatrix}-0.443 & -0.039\\ 0.014 & -0.432\end{bmatrix}$, $\Gamma = [G_m] = \begin{bmatrix}0.15 & 0\\ 0 & 0.15\end{bmatrix}$ and $H = \begin{bmatrix}1 & 0\\ 0 & 1\end{bmatrix}$. An ordinary augmented formula is derived from Equation (26) using new variables $x_h^{+}(k) = \begin{bmatrix}\Delta s^{+}(k) & \underset{\sim}{y}^{+}(k)\end{bmatrix}^{T}$ [4].

$$\begin{aligned}
\overbrace{\begin{bmatrix}\Delta s_{k+1}^{+}\\ \underset{\sim k+1}{y^{+}}\end{bmatrix}}^{x_h(k+1)} &= \overbrace{\begin{bmatrix}\Omega_{m\times m} & 0_{m\times q}\\ H\Omega_{q\times m} & I_{q\times q}\end{bmatrix}}^{A_h}\overbrace{\begin{bmatrix}\Delta s_{k}^{+}\\ \underset{\sim k}{y^{+}}\end{bmatrix}}^{x_h(k)} + \overbrace{\begin{bmatrix}\Phi_{m\times n}\\ H\Phi_{q\times n}\end{bmatrix}}^{B_h}\Delta\bar{u}_{k}^{+} + \overbrace{\begin{bmatrix}\Gamma_{m\times n}\\ H\Gamma_{q\times n}\end{bmatrix}}^{E_h}\underset{\sim k}{\varepsilon^{+}}\\
\underset{-k}{y^{+}} &= \overbrace{\begin{bmatrix}0_{q\times m} & I_{q\times q}\end{bmatrix}}^{C_h}\begin{bmatrix}\Delta s_{k}^{+}\\ \underset{\sim k}{y^{+}}\end{bmatrix}
\end{aligned} \tag{27}$$

Np and *Nc* are defined as the prediction of the sliding status deviation and control horizon step. Formula (27) uses the horizon range to expand the difference sliding sequences based on predictive control inputs as

$$\begin{aligned}
\underset{-}{y}^{+}(k+N_P|k) &= C_hA_h{}^{Np}x_h^{+}(k) + C_hA_h{}^{Np-1}B_h\Delta\bar{u}^{+} + C_hA_h{}^{Np-1}E_h\underset{\sim}{\varepsilon}^{+}(k)\\
&+C_hA_h{}^{Np-2}B_h\Delta\bar{u}^{+}(k+1) + C_hA_h{}^{Np-2}E_h\underset{\sim}{\varepsilon}^{+}(k+1) + \cdots\\
&+C_hA_h{}^{Np-Nc}B_h\Delta\bar{u}^{+}(k+Nc-1) + C_hE_h\underset{\sim}{\varepsilon}^{+}(k+Np-1)
\end{aligned} \tag{28}$$

Define the predicted output of sliding, subsequent series of control, and deviation of disturbances arrays as

$$\begin{aligned}
&\bar{y}^{+}(k) = \begin{bmatrix}\underset{-}{y}^{+}(k+1|k)\cdots\underset{-}{y}^{+}(k+Np|k)\end{bmatrix}^{T} \in \Re^{Np}, \qquad \Delta\bar{x}_h^{+}(k) = \begin{bmatrix}\Delta x_h^{+}(k+1|k)\cdots\Delta x_h^{+}(k+Np|k)\end{bmatrix}^{T} \in \Re^{Np}\\
&\Delta\bar{u}^{+}(k) = \begin{bmatrix}\Delta\bar{u}^{+}(k|k)\cdots\Delta\bar{u}^{+}(k+Nc-1|k)\end{bmatrix}^{T} \in \Re^{N_{c,u}}, \qquad \bar{\varepsilon}^{+}(k) = \begin{bmatrix}\underset{\sim}{\varepsilon}^{+}(k|k)\cdots\underset{\sim}{\varepsilon}^{+}(k+Np-1|k)\end{bmatrix}^{T} \in \Re^{Np,\varepsilon}
\end{aligned} \tag{29}$$

The compact form of equivalent output progressions under prediction is derived as

$$\bar{y}^{+}(k) = E.\bar{x}_h^{+}(k) + M.\Delta\bar{u}^{+}(k) + \Lambda.\bar{\varepsilon}^{+}(k) \tag{30}$$

The associated matrices of sliding law in Equation (30) can be defined as

$$E = \begin{bmatrix}C_hA_h \cdots C_hA_h{}^{Np}\end{bmatrix}^{T}, M = \begin{bmatrix}C_hB_h & 0 & \cdots & 0\\ C_hA_hB_h & C_hB_h & \cdots & 0\\ \vdots & \vdots & \ddots & \vdots\\ C_hA_h{}^{Np-1}B & C_hA_h{}^{Np-2}B_h & \cdots & C_hA_h{}^{Np-Nc}B_h\end{bmatrix}, \Lambda = \begin{bmatrix}C_hE_h & 0 & \cdots & 0\\ C_hA_hE_h & C_hE_h & \cdots & 0\\ \vdots & \vdots & \ddots & \vdots\\ C_hA_h{}^{Np-1}E_h & C_hA_h{}^{Np-2}E_h & \cdots & C_hE_h\end{bmatrix} \tag{31}$$

Minimization rule of the cost function based on problem Equation (30) is defined as [4]

$$\begin{aligned}
&J(k) = \sum_{i=1}^{Np}\left\|y^{ref}(k+i|k) - y(k+i|k)\right\|_{G_i}^{2} + \sum_{i=0}^{Nc-1}\left\|\Delta u(k+i|k)\right\|_{Io_i}^{2}\\
&\text{st} \quad \Delta u_{\min} \le \Delta\bar{u}^{+}(k) \le \Delta u_{\max}, \quad \Delta y_{\min} \le \Delta\bar{y}^{+}(k) \le \Delta y_{\max}
\end{aligned} \tag{32}$$

where y^{ref} is the items of desired input, y is the items of output progressions, Io and G are the + definite weight matrices within a restricted range of input/output. The restriction term $\hat{\Delta}_d$ in Equation (25) is a quasi-sliding value that makes the sliding response close to the sliding path in a short step and also removes chattering behavior [35, 36].

The complete control law is comprised of Rc unit as

$$u^{+}_{rdq} = u^{+}_{Rc,dq} + U^{+}_{k,dq} \tag{33}$$

The discrete-time Tustin paradigm-based second-degree double-task integral compensation Rc unit is connected with the PSMC in a parallel connection.

$$R_c = \mathrm{sK}_{ro}/(\mathrm{s}^2 \mp (\pm 6.\omega_e)^2)\Big|_{s=\frac{2}{Tg}\frac{z-1}{z+1}} \tag{34}$$

The gains of Rc unit are defined as Kro_d= 56.3 and Kro_q= 43.8. Thus, the magnitude against the 300 Hz is 30.1 dB within the inversion points around $\pm 90^o$ in the Bode curve based on the resonant unit, as shown in Figure 8(a). The PSMC-R and open-loop path Bode curve in Figure 8(b) and Figure 8(c)for P_s show that the magnitude at 300 Hz are (32.3dB) with the phase degree swing around 0^o, and (98.6dB) with the phase degree swing around -90^o respectively. Thus, these characteristics of magnitude and phase values are broad enough to decrease the control deviation and suit the compensation mechanism. Moreover, the multiple complicated-coefficients filter MCCF used to extract the main signals and their harmonic chains for the overall system under the supply distortion [37], as shown in Figure 9.

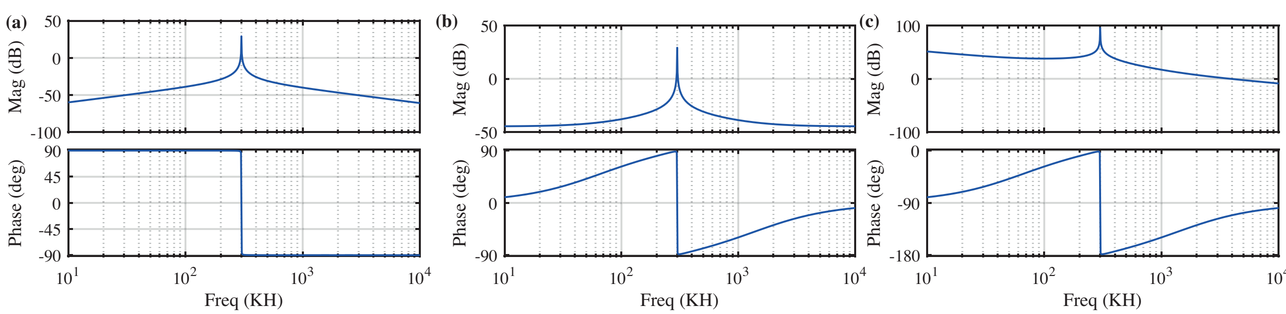

Figure 8. Bode spectrum of (a) resonant function (b) PSMC-R controller (c) open control-loop trajectory.

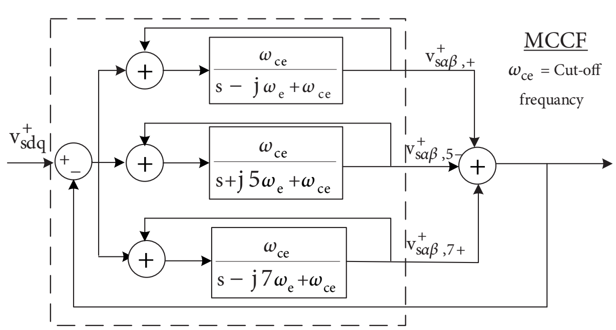

Figure 9. MCCF filter with a cut-off frequency ω_{ce}.

4. Analysis of the results

According to the general schematic diagrams of DFIG-WPGS in Figure 10, the control unit PSMC-R is presented with its internal connections, as shown in Figures 11 and 12. The rated DFIG parameters and quantities are defined in Table 1.

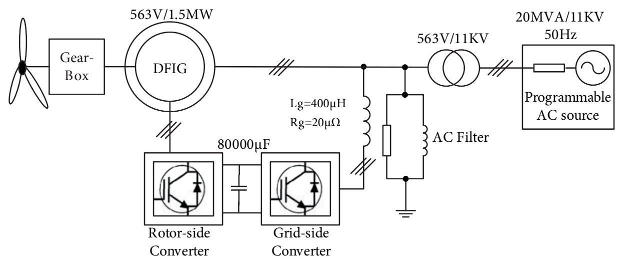

Figure 10. The public diagram of DFIG-WPGS.

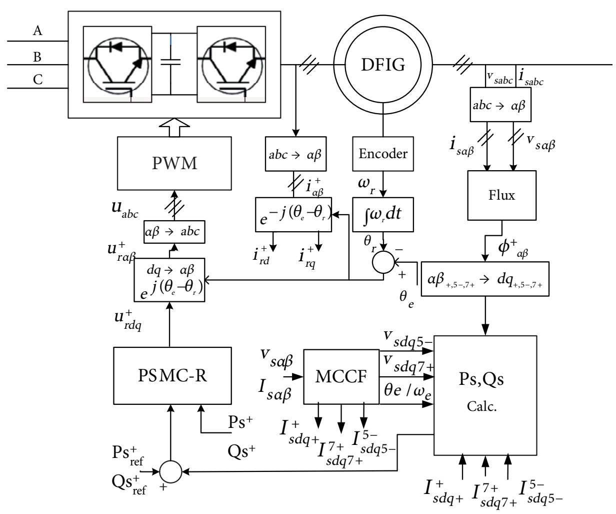

Figure 11. Diagram of the PSMC-R technique for the DFIG.

Table 1. The rated DFIG-WPGS and PSMC-R quantities are used in the simulation.

Parameter	**Value**	**Parameter**	**Value**	**Parameter**	**Value**
Ps	1.5 MW	**Qs**	0 MW	**Vs**	563V
Converters Freq.	2.5kHz	**fs**	50Hz	**Rs/Rr**	2.6e-3/2.9e-3Ω
Ls/Lr/Lm	2.6/2.6/2.5 mH	**J**	$28kgm^2$	**No.pole pair**	4
Kro_d/Kro_q	56.3/43.8	**PIR(Kp,Ki,Kr)**	0.35/0.24/1.5	**PI (Kp,Ki)**	0.52/0.63
Rotor Speed	1630 r/min-1.086 pu	**Hp**	10	**Hc**	3
HPI rate case-1,3 &4	(4% and 3%)	**HPI rate case-2**	(5%)	**Run Time**	1.25 s

The regulator principle for DC-tied voltage is designed based on a bidirectional-tied converter toward network-port based on the space vector modification SVM standards to conform to the approach described in [38]. Figure 13 illustrated that the system responses depend on different control types, identified along the time

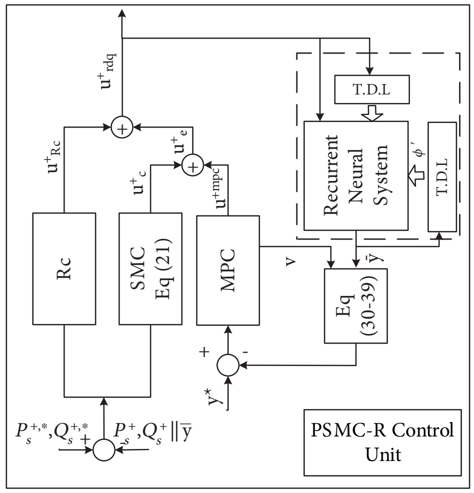

Figure 12. The internal connections of the PSMC-R control unit.

from 0 to 1.25 s while the harmonic regulator unit is inactive within 0-0.5 s for the PI regulator. At the interval time 0-1 s, the traditional PI, PIR-Naslin, and SMC control are applied to the system during the occurred harmonic condition. Also, after 1 s is depleted, the offered PSMC-R control at $+dq$-level is allowed to control the stator-port power during harmonic growth. However, within the time interval classified as a PI regulator and before the submitted control approach for harmonic, the graphical results in Figures 13 confirmed that the regular controller is unreliable in dealing with harmonic sequence components on the stator power dq-reference level. Thus, the stator-port current is exceedingly malformed that is exhibited in Figure 13(c). Furthermore, the active 300 Hz oscillation is provided momentarily on stator-port power and MT in Figure 13 (a, b and g).

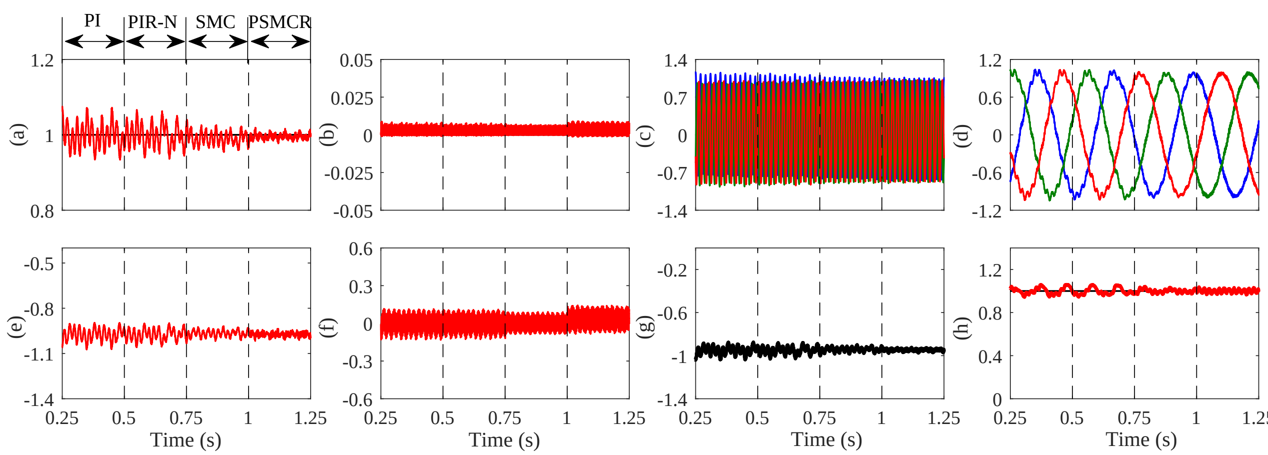

Figure 13. The results as (pu) for 4% and 3% of 5th/7th harmonic types during distorted voltage (a) active power, (b) reactive power, (c) AC stator-port currents, (d) AC rotor-port currents (e) $+d$-axis rotor-port current., (f) $+q$-axis rotor-port current, (g) generator electromagnetic torque, (h) DC-link voltage.

In Figure 14, the effect of PI without the harmonic regulator unit is shown as the spectral range of the harmonic sequence versus frequency range during the 0-0.5 s time range for the stator- and rotor-port current. Due to the feeder voltage deformation, the $5^{th}/7^{th}$-degree harmonic series at frequency 250/350 Hz are also originated in stator-port current and magnetic intensity into the machine air slots. In Figure 13 (d), the AC rotor current actual frequency of 5 Hz is produced from these characteristics and involves harmonic sequences with corresponding frequencies of 295 Hz and 305 Hz for types 5^{th} and 7^{th}-degree, respectively influences rotor-port waveform. When the PIR-Naslin, SMC, and PSMC-R were enabled at 0.5, 0.75, and 1 s, respectively, as formed in Figures 13 (a and b), the (+) successions of primary and harmonic items with (5^{th}-/7^{th}-types) are produced on the stator power that conveniently adapted with fast response growth. Explicitly, the harmonic components of stator power based on offered controller achieved a low tracking error conduct between the desired signals and estimated performance. To view the preference of PSMC-R, the max-oscillation rate of Ps and Qs associated with 300 Hz, the $5^{th}/7^{th}$-degree sequences terms of harmonics on stator current, rotor current associated with 5 Hz, electromagnetic torque, and the DC-voltage, are scheduled clearly in Table 2. The PSMC-R mechanism is capably attaining the control functions, as shown in Figures 13 and Table 2. Furthermore, the desired and dynamic reaction has achieved a good tracking error while decreasing 5 Hz-harmonic waves for the rotor current. Also, it presented high mitigation in MT pulsations associated with 300 Hz and $5^{th}/7^{th}$-degree harmonics on stator-port active power and current, which presents the regular heating process in the rotor windings while reducing the losses associated with harmonics waves.

Table 2. Results of comparative analysis for different control mechanisms.

HPI,Pulsation (%)	**PI**	**PIR**	**SMC**	**PSMC-R**
Is 5$_{th}$	±4.90	±3.16	±1.91	±0.54
Is 7$_{th}$	±4.40	±2.36	±1.83	±0.52
Ir29$_{th}$	±3.10	±3.40	±1.60	±0.52
Ir30$_{th}$	±3.40	±3.10	±1.89	±0.90
Ps	±4.71	±4.34	±2.46	±1.08
Qs	±7.24	±4.22	±4.01	±2.06
Te	±7.42	±5.20	±2.97	±1.48
V$_{dc}$	±6.03	±4.70	±2.47	±2.03

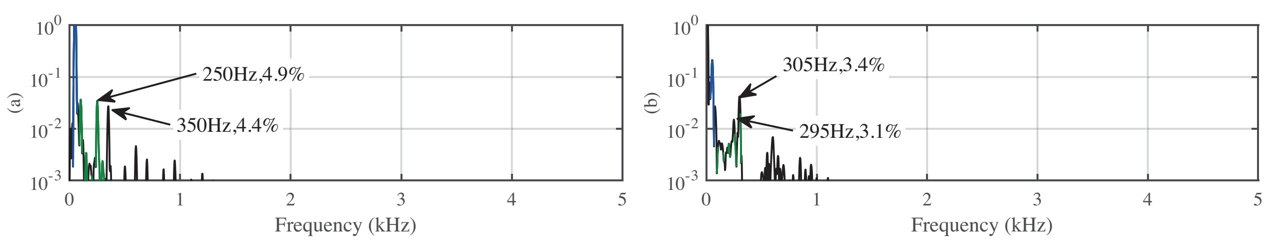

Figure 14. Harmonic curve for (a) stator-port current at 50 Hz), (b) rotor-port current at 5 Hz).

Further assessment is presented during 5% ratio for each $5^{th}/7^{th}$-type HPI on voltage in Figure 15. As shown in Figure 15, immediately after voltage distortions occur at 1 s, the compensation function inside the PSMC-R accurately regulates 300 Hz components related to the $-5\ \omega_e$ and $7\omega_e$ hesitations at the $+dq$-reference level attenuate the introduced harmonics. The PSMC-R control gives smoother fluctuations for the model responses, especially for stator power and MT during the distortions of the network voltage in Figures 15 (a, b and g), respectively. Besides, the fluctuation rates of dq-stator-port active/reactive power and MT are around (±1.46, ±3.1, ±4.66 and ±5.11%), (±1.26, ±3.55, ±4.38 and ±4.48%), (±2.19, ±3.73, ±5.64, and ±6.18%), respectively, whereas, the average of DC voltage fluctuation is (±1.98, ±2.44, ±3.89 and ±4.32%) for PSMC-R, SMC, PIR-Naslin and PI, as shown in Figure 15 (h). Also, Figures 15 (e and f) offer that the oscillation rates of the dq-rotor current are (±3.2, ±3.95, ±6.41, and ±7.26%) and (±2.96, ±4.31, ±4.88 and ±5.99%) for the PSMC-R, SMC, PIR-Naslin and PI, respectively.

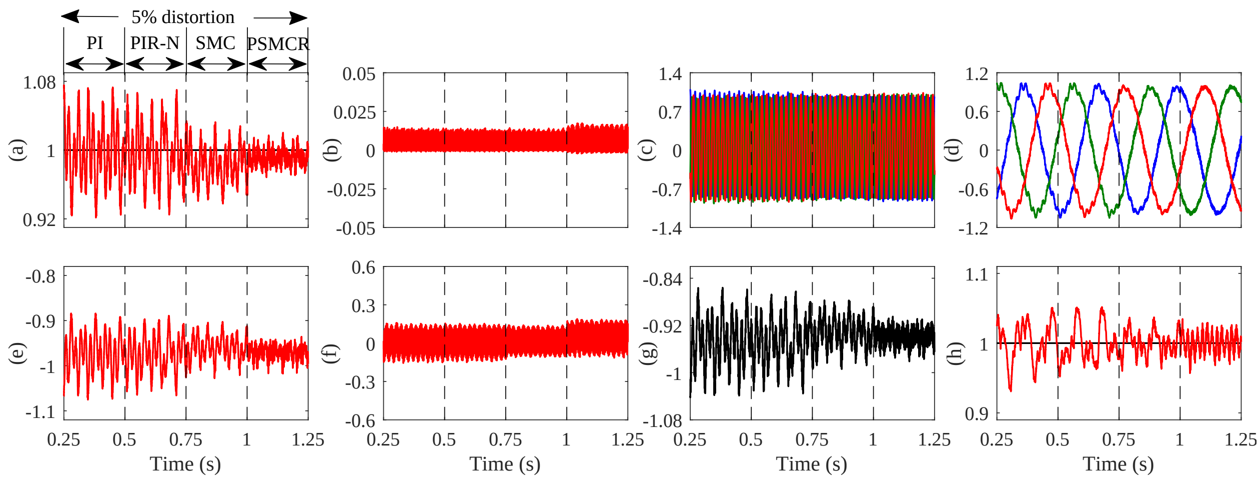

Figure 15. The results as (pu) for 5% of $5^{th}/7^{th}$ harmonic types during distorted voltage (a) active power, (b) reactive power, (c) AC stator-port currents, (d) AC rotor-port currents (e) $+d$-axis rotor-port current, (f) $+q$-axis rotor-port current, (g) generator electromagnetic torque, (h) DC-link voltage.

In the real-time running of WPG, the wind speed is frequently changing, and the turbine speed controller may not provide a fast response to an abrupt change in the four operating regions. That may lead to reducing the efficiency or damaging the system equipment. PSMC-R strategy is applied with a down-/upward slope of the rotor speed between 1640 and 1170 rev/min (1.093 pu – super-synchronous to 0.8 pu sub-synchronous mode). The downward region occurred at the time interval 0.4-1.05 s shown in Figure 16(b). The stator voltage maintains the $5^{th}/7^{th}$ HPI values as 4% and 3%. The emulated power response in Figure 16 explained that the provided method carried out better dynamic performance through numerous degrees of rotor speed. The rate of an amount attributed to stator-port active power and ETM was decreased from 1 to 0.73 pu with an increasing oscillation ratio from 2.2% to 10.2%, and 1 to 0.71 pu with increasing oscillation ratio from 2.6% to 16.5% at the interval time 0.4-1 s, respectively, as in Figure 16 (a, b and g). As seen, under the introduced control system, an increase in 300 Hz wave signals appeared as high ripples on the produced stator power and MT signals during the harmonics deformation with changed speed. In Figure 16, the PSMC-R regulator gave a good performance during numerous of rotor-port speed degrees and ripples of the torque stress on the generator. Figures 16 (e and f) illustrated that the current capacitance ratio of the rotor-port decreased by about 50.6%, with the oscillation ratio increasing from 3.2% to 19.2% in the interval time of 0.4-1 s, respectively. Also, in Figures 16, the PSMC-R carried out good tracking performance of stator power, stator, and rotor current at ($+dq$) reference level, with smaller overshot, less current oscillation ripple during 100% of stator power and fast response during variation of rotor speed. Besides, PSMC-R maintained constant sequence periods for stator current and proper DC voltage tracking at its nominal path; meantime, it has adapted the sequence for rotor current at 0.4 and 1 s, as in Figures 16 (c, h and d), respectively. Further dynamic analysis of the PSMC-R is achieved during the wind movement variation between cut-in and the rated speed (15 m/s) along 0.4-2 s, as shown in Figure 17 (a). In Figure 17 (c and d), the regulation units of DFIG-WPGS generate a low value of the generator power and torque that swing at 0.25 pu and -0.3 pu around the cut-in wind speed along (0.4-1 s and 1.5-2 s) respectively, based on the selection mechanism of the maximum power. Besides, when the wind movement increases with a sufficient speed to allow the WT to run in the classified speeds range, the DFIG-WPGS can deliver the power toward the grid and increase the generator torque to swing around the nominal values along 1-1.5 s.

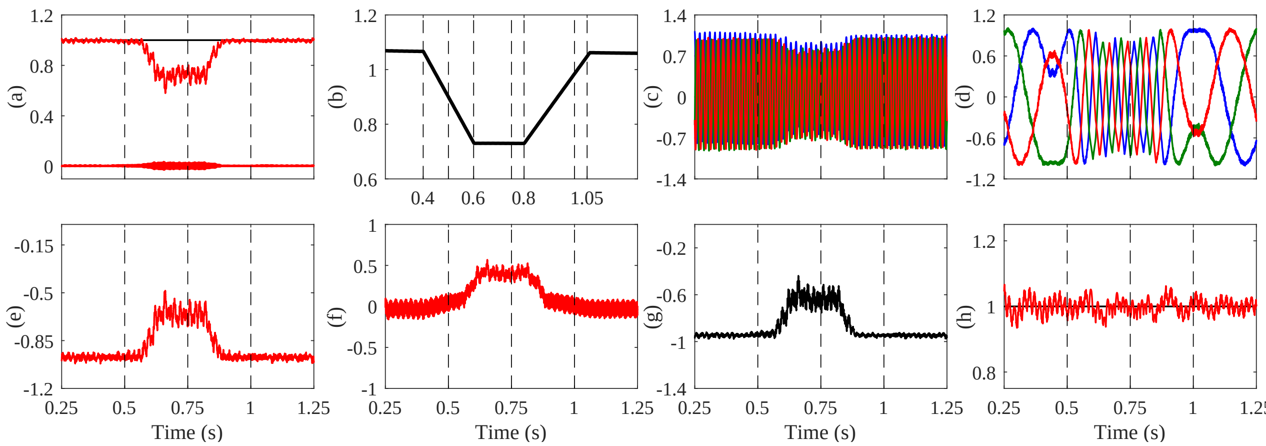

Figure 16. The results as (pu) during changing in the rotor- velocity (a) active and reactive power, (b) rotor-port velocity, (c) AC stator-port currents, (d) AC rotor-port currents (e) $+d$-axis rotor-port current, (f) $+q$-axis rotor-port current, (g) generator electromagnetic torque, (h) DC-link voltage.

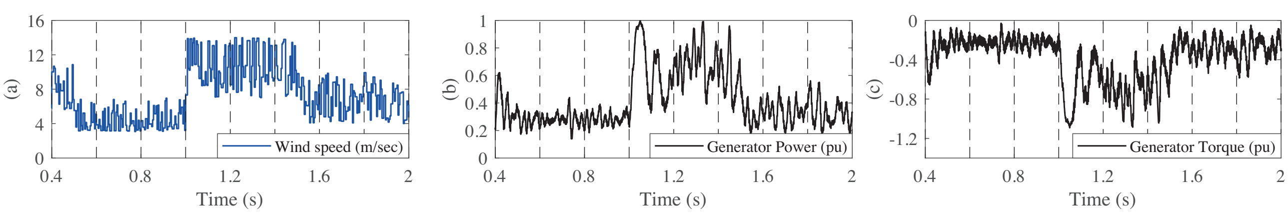

Figure 17. Dynamic results based on (a) wind profile that changes between cut-in speed ($3.5m/s$) and nominal speed ($15m/s$), (b) generator power (pu), (c) generator torque (pu).

The parameters variation test is performed by assuming that coil inductance parameters are changed based on the inherent variations in the interior machine magnetic behavior during sudden operating changes. Besides, the expected changing resistors values of stator and rotor are involved while discarding their windings leakage differences. This test offered PSMC-R during the same hypothesis in the first dynamic test. In Figure 18, the mutual inductor and stator/rotor resistor coefficients values are decreased -50% in the FC-I test, and also -50% and +50% are included to mutual inductor and resistors in FC-II test respectively, besides +50% has been added to all specified coefficients in FC-III test. In general, Figures 18 (a, b and g) show that the PSMC-R mechanism gives smoother fluctuation rates of the stator-port active/reactive power and MT around (2.09%, 1.3%, 2.0%, and 1.6%), (2.87%, 3.21%, 3.1%, and 3.02%), (2.84%, 3.4%, 2.51%, and 2.9%) for the NC, FC (I,II,III) tests respectively. Whereas, the average of DC voltage fluctuation is (3.91%, 3.56%, 3.3%, and 3.02%)

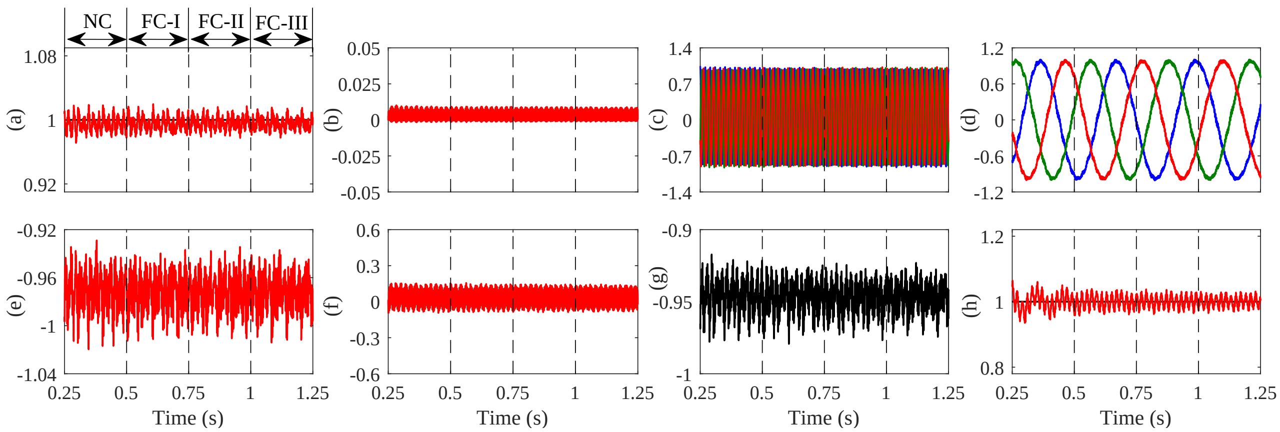

Figure 18. The results as(pu) with various parameters alterations for (a) active power, (b) reactive power, (c) AC stator-port currents, (d) AC rotor-port currents (e) $+d$-axis rotor-port current, (f) $+q$-axis rotor-port current, (g) generator electromagnetic torque, (h) DC-link voltage.

for the NC, FC (I,II,III) tests, as shown in Figure 18 (h) respectively. Also, Figures 18 (e) to (f) offer that the oscillation rates of the dq-rotor current are (4.6%, 5.1%, 5.02%, and 4.7%) and (8.21%, 7.7%, 8.8%, and 8.6%) for the NC, FC (I,II,III) tests, respectively. All results demonstrate that the dynamic realization of the proposed PSMC-R gave satisfactory durability during the extreme changes of the stator, rotor, and combined inductive parameters.

5. Conclusion

This topic has discussed PSMC-R that contains predictive sliding chattering signals based on the deep-recurrent neural network for the stator-port power model of the nonlinear DFIG-WPG under 5^{th} and 7^{th}-degree deformation voltage. The PSMC-R finds the optimum variables with different process modes by reformulating the conventional SMC based on the required power using a predictive term to expect the best points in the sliding plane using the quadratic algorithm module feature plus compensation unit. Simulation results showed that the designed prediction algorithm-based sliding chatter law of the SMC-R approach presented the best dynamic tracking and low overshoot and fluctuation of energy quantities compared to classical control approaches during various operation terms. Besides, the frequency of stator-port sinusoidal current wave has remained constant. Also, the components of stator-port power collected from basic and 5^{th} and 7^{th}-degree are promptly manipulated using the PSMC-R approach to avoid successive dismantling of the components.

References

[1] REN21. Renewables 2019 global status report. REN21 Secretariat: Paris, France 2019.

[2] Hemeyine AV, Abbou A, Bakouri A, Mokhlis M, Moustapha El et al. A robust interval Type-2 fuzzy logic controller for variable speed wind turbines based on a doubly fed induction generator. Inventions 2021; 6 (2): 21. doi: 10.3390/inventions6020021

[3] Brando G, Dannier A, Spina I. Performance analysis of a full order sensorless control adaptive observer for doubly-fed induction generator in grid connected operation. Energies 2021; 14 (5): 1254. doi: 10.3390/en14051254

[4] Liu X, Kong X. Nonlinear model predictive control for DFIG-based wind power generation. IEEE Transactions on Automation Science and Engineering 2014; 11 (4): 1046-1055. doi: 10.1109/TASE.2013.2284066

[5] Da Costa JP, Pinheiro H, Degner T, Arnold G. Robust controller for DFIGs of grid-connected wind turbines. IEEE Transactions on Industrial Electronics 2011; 58 (9): 4023-4038. doi: 10.1109/TIE.2010.2098630

[6] Goodarzi A, Ranjbar AM, Dehghani M, GhasemiGarpachi M, Ghiasi M. Doubly fed induction generators to enhance inter-area damping based on a Robust controller: H_2/H_∞ Control. SN Applied Sciences 2021; 3 (1): 1-14. doi: 10.1007/s42452-021-04150-1

[7] Zhang Y, Jiao J, Xu D, Jiang D, Wang Z et al. Model predictive direct power control of doubly fed induction generators under balanced and unbalanced network conditions. IEEE Transactions on Industry Applications 2020; 56 (1): 771-786. doi: 10.1109/TIA.2019.2947396

[8] Marques GD, Iacchetti MF. Minimization of torque ripple in the DFIG-DC system via predictive delay compensation. IEEE Transactions on Industrial Electronics 2018; 65 (1): 103-113. doi: 10.1109/TIE.2017.2716860

[9] Vayeghan MM, Davari SA. Torque ripple reduction of DFIG by a new and robust predictive torque control method. IET Renewable Power Generation 2017; 11 (11): 1345-1352. doi: 10.1049/iet-rpg.2016.0695

[10] Zhang X, Hou B. Double vectors model predictive torque control without weighting factor based on voltage tracking error. IEEE Transactions on Power Electronics 2018; 33 (3): 2368-2380. doi: 10.1109/TPEL.2017.2691776

[11] Cheng C, Nian H. Low-complexity model predictive stator current control of DFIG under harmonic grid voltages. IEEE Transactions on Energy Conversion 2017; 32 (3): 1072-1080. doi: 10.1109/TEC.2017.2694849

[12] Sun D, Wang X, Nian H, Zhu ZQ. A sliding-mode direct power control strategy for DFIG under both balanced and unbalanced grid conditions using extended active power. IEEE Transactions on Power Electronics 2018; 33 (2): 1313-1322. doi: 10.1109/TPEL.2017.2686980

[13] Patnaik RK, Dash PK. Fast adaptive back-stepping terminal sliding mode power control for both the rotor-side as well as grid-side converter of the doubly fed induction generator-based wind farms. IET Renewable Power Generation 2016; 10 (5): 598-610. doi: 10.1049/iet-rpg.2015.0286

[14] Martinez MI, Tapia G, Susperregui A, Camblong H. Sliding-mode control for DFIG rotor- and grid-side converters under unbalanced and harmonically distorted grid voltage. IEEE Transactions on Energy Conversion 2012; 27 (2): 328-339. doi: 10.1109/TEC.2011.2181996

[15] Eltamaly AM, Al-Saud MS, Abo-Khalil AG. Dynamic control of a DFIG wind power generation system to mitigate unbalanced grid voltage. IEEE Access 2020; 8: 39091-39103. doi: 10.1109/ACCESS.2020.2976195

[16] Sun D, Wang X. Sliding-mode DPC using SOGI for DFIG under unbalanced grid condition. Electronics Letters 2017; 53(10): 674-676. doi: 10.1049/el.2017.0963

[17] Nian H, Cheng P, Zhu ZQ. Coordinated direct power control of DFIG system without phase-locked loop under unbalanced grid voltage conditions. IEEE Transactions on Power Electronics 2016; 31 (4): 2905-2918. doi: 10.1109/TPEL.2015.2453127

[18] Hu J, Nian H, Hu B, He Y, Zhu ZQ. Direct active and reactive power regulation of DFIG using sliding-mode control approach. IEEE Transactions on Energy Conversion 2010; 25 (4): 1028-1039. doi: 10.1109/TEC.2010.2048754

[19] Martinez MI, Susperregui A, Tapia G, Xu L. Sliding-mode control of a wind turbine-driven double-fed induction generator under non-ideal grid voltages. IET Renewable Power Generation 2013; 7 (4): 370-379.

[20] Xiong L, Li P, Wang J. High-order sliding mode control of DFIG under unbalanced grid voltage conditions. International Journal of Electrical Power & Energy Systems 2020; 117: 105608. doi: 10.1016/j.ijepes.2019.105608

[21] Djilali L, Sanchez EN, Belkheiri M. First and high order sliding mode control of a DFIG-based wind turbine. electric power components and systems 2020; 48(1-2): 105-116. doi: 10.1080/15325008.2020.1758836

[22] Chen SZ, Cheung NC, Chung Wong K, Wu J. Integral sliding-mode direct torque control of doubly-fed induction generators under unbalanced grid voltage. IEEE Transactions on Energy Conversion 2009; 25 (2): 356-368. doi: 10.1109/TEC.2009.2036249

[23] Shang L, Hu J. Sliding-mode-based direct power control of grid-connected wind-turbine-driven DFIG under unbalanced grid voltage conditions. IEEE Transactions on Energy Conversion 2012; 27 (2): 362-373. doi: 10.1109/TEC.2011.2180389

[24] Hao X, Yang X, Liu T, Huang L, Chen W. A sliding-mode controller with multi-resonant sliding surface for single-phase grid-connected VSI with an LCL filter. IEEE Transactions on Power Electronics 2013; 28 (5): 2259-2268. doi: 10.1109/TPEL.2012.2218133

[25] Quan Y, Hang L, He Y, Zhang Y. Multi-Resonant-based sliding mode control of DFIG-based wind system under unbalanced and harmonic network conditions. Applied Sciences 2019; 9 (6): 1124. doi: 10.3390/app9061124

[26] Hu J, Nian H, Xu H, He Y. Dynamic modeling and improved control of DFIG under distorted grid voltage conditions. IEEE Transactions on Energy Conversion 2011; 26 (1): 163-175. doi: 10.1109/TEC.2010.2071875

[27] Shi K, Yin X, Jiang L, Liu Y, Hu Y et al. Perturbation estimation based nonlinear adaptive power decoupling control for DFIG wind turbine. IEEE Transactions on Power Electronics 2020; 35 (1): 319-333.

[28] Mohammed OME, Xu W, Liu Y, Blaabjerg F. An improved control method for standalone brushless doubly fed induction generator under unbalanced and nonlinear loads using dual-resonant controller. IEEE Transactions on Industrial Electronics 2021; 68 (7): 5594-5605. doi: 10.1109/TIE.2020.2994891

[29] Wu C, Zhou D, Blaabjerg F. Direct power magnitude control of DFIG-DC system without orientation control. IEEE Transactions on Industrial Electronics 2021; 68 (2): 1365-1373. doi: 10.1109/TIE.2020.2970666

[30] Kuzenkov O, Kuzenkova G. Identification of the fitness function using neural networks. Procedia Computer Science 2020; 169: 692-697. doi: 10.1016/j.procs.2020.02.179

[31] Yan Z, Wang J. Model predictive control of nonlinear systems with unmodeled dynamics based on feedforward and recurrent neural networks. IEEE Transactions on Industrial Informatics 2012; 8 (4): 746-756.

[32] Du H, Yu X, Chen M, Li S. Chattering-free discrete-time sliding mode control. Automatica, 2016; 68(c): 87-91. doi: 10.1016/j.automatica.2016.01.047

[33] Su X, Liu X, Shi P, Yang R. Sliding mode control of discrete-time switched systems with repeated scalar nonlinearities. IEEE Transactions on Automatic Control 2017; 62(9): 4604-4610. doi: 10.1109/TAC.2016.2626398

[34] Yu S, Long X. Finite-time consensus for second-order multi-agent systems with disturbances by integral sliding mode. Automatica 2015; 54: 158-165. doi: 10.1016/j.automatica.2015.02.001

[35] Xu Q, Li Y. Model predictive discrete-time sliding mode control of a nano-positioning piezo-stage without modeling hysteresis. IEEE Transactions on Control Systems Technology 2012; 20 (4): 983-994. doi: 10.1109/TCST.2011.2157345

[36] Bartoszewicz A. Discrete-time quasi-sliding-mode control strategies. IEEE Transactions on Industrial Electronics 1998; 45 (4): 633-637. doi: 10.1109/41.704892

[37] Terriche Y, Golestan S, Guerrero JM, Vasquez JC. Multiple-complex coefficient-filter-based PLL for improving the performance of shunt active power filter under adverse grid conditions. IEEE Power & Energy Society General Meeting 2018; 1-5. doi: 10.1109/PESGM.2018.8586172

[38] Hu JB, Zhang W, Wang HS, He Y, Xu L. Proportional integral plus multi-frequency resonant current controller for grid-connected voltage source converter under imbalanced and distorted supply voltage conditions. Zhejiang University-SCIENCE A 2009; 10 (10): 1532-1540. doi: 10.1631/jzus.A0820440